Evaluation and Suppression of Oscillations in Inductive Power Transfer Systems with Constant Voltage Load and Pulse Skipping Modulation

Jiayu Zhou, Giuseppe Guidi Kjell Ljøkelsøy Jon Are Suul

***Abstract*— This paper identifies how Constant Voltage Load (CVL) characteristics cause Inductive Power Transfer (IPT) systems to exhibit a poorly damped oscillation mode. When operated with pulse skipping strategies such as Pulse Density Modulation (PDM), the skipped voltage pulses can excite this mode and cause severe oscillations that do not appear in systems with a constant resistance load (CRL). The critical mode is identified from a linearized state-space model of the system and two control approaches are proposed for attenuating the oscillations in current amplitude and power flow. Firstly, the influence of the operating frequency on the critical eigenvalue is analyzed and it is shown how slightly off-resonant operation can increase the damping of the oscillation mode. Secondly, an active damping method based on sending current feedback control is studied. The active damping is based on phase shift modulation with limited phase shift angles applied to the PDM signal when oscillations are detected. The effectiveness and feasibility of the proposed methods are validated by simulations and experimental results from a small-scale laboratory prototype.**

Keywords—Constant voltage load, inductive power transfer, oscillation damping, pulse density modulation, small-signal model

I. INTRODUCTION

Wireless inductive power transfer (IPT) systems are being increasingly utilized for a wide range of applications, such as wireless power supplies and battery chargers for cell phones [1], electric vehicles [2], and marine transports [3]. In practical applications, a constant voltage load (CVL) or slowly varying load voltage will be the most common receiving side interface for battery charging. For analysis of steady-state operation, and for efficiency optimization, such systems are usually modelled with an equivalent constant resistance load (CRL) [4]-[8]. However, the dynamic characteristics of CVL and CRL conditions are different, which implies that CRL models should not be used for dynamic studies and control system design of battery charging systems [9]-[10].

For IPT applications intended to handle large variations in power transfer and/or coupling conditions, a dynamic model including an accurate representation of the load side is necessary to analyse the dynamical characteristics and to design the control loops. Thus, examples of state-space models developed for representing the dynamic characteristics of the IPT systems with CVL have been presented in [9]-[10]. In [9] the differences in the dynamic response to voltage variations with CVL and equivalent CRL models are also explicitly demonstrated. The results clearly showed how the CVL model always exhibits a response with significantly lower damping than the CRL model.

A first analysis of how the differences in dynamic characteristics between CVL and CRL systems influence the response to the modulation strategy was presented in [13]. Specifically, it was shown how pulse density modulation (PDM) [14]-[18] can cause large oscillations in currents and power flow when the skipped voltage pulses are exciting the poorly damped oscillation mode that can be identified by the model from [9] and [10]. From previous literature on oscillations in resonant converters operated with PDM, the general mitigation approach has been to reduce the excitation of the poorly damped oscillation mode by applying enhanced pulse density modulation (EPDM) to limit the variations in the sending-side voltage [25]. However, it was demonstrated in [13] that large current/power ripples can still appear in IPT systems with CVL at certain pulse densities due to the extremely low system damping. To mitigate such oscillations, [13] also proposed an active damping method based on transiently superimposing Phase Shift Modulation (PSM) to the pulse pattern generated by the PDM.

In this paper, the analysis from [13] is expanded by further evaluation of the root cause and worst-case conditions for oscillations in CVL IPT systems with PDM. Furthermore, two approaches for increasing system damping by control are evaluated. First, an analysis of how the operating frequency can influence the damping of the critical oscillation mode is introduced, and it is shown that the damping can be increased at slightly sub-resonant frequencies. However, to ensure zero voltage switching (ZVS) in the full working range, the operating frequency of the system cannot be significantly reduced, making it difficult to increase the system damping

Parts of this paper were presented at the the Thirteenth Annual IEEE Energy Conversion Congress and Exposition, ECCE 2021, Vancouver, British Columbia, Canada (Virtually), 10-14 October 2021, with the title "Analysis and Mitigation of Oscillations in Inductive Power Transfer Systems with Constant Voltage Load and Pulse Density Modulation" This work was conducted within the project "Ultra-high power density wireless charging for maritime applications," supported by the Research Council of Norway under Project number 294871. *(Corresponding author: Jon Are Suul.)*

J. Zhou is with the Department of Engineering Cybernetics, NTNU, 7491 Trondheim, Norway, jiayu.zhou@ntnu.no

G. Guidi and K. Ljøkelsøy are with SINTEF Energy Research, 7465 Trondheim, Norway, Giuseppe.Guidi@sintef.no, Kjell.Ljokelsoy@sintef.no

J. A. Suul is with the Department of Engineering Cybernetics, NTNU, 7491 Trondheim, Norway, and also with SINTEF Energy Research 7491 Trondheim, Norway, jon.are.suul@ntnu.no

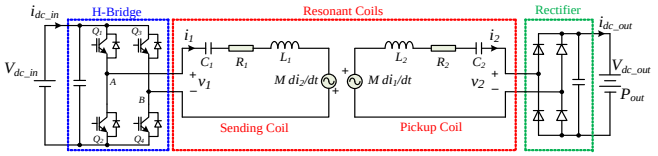

Fig. 1. Series-series compensated IPT system with constant voltage load

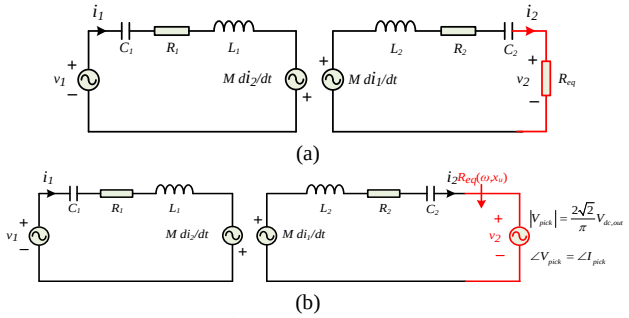

(a)

(b)

Fig. 2. Equivalent circuits of SS-compensated IPT system using harmonic approximation. (a) CRL model (b) CVL model.

enough for suppressing oscillations in all operating conditions. Therefore, the design of active damping control by transiently introducing PSM, as proposed in [13], is discussed in detail. Finally, to achieve good damping in all operating conditions with limited control effort, it is proposed to operate the IPT system at the slightly sub-resonant frequency with a combination of EPDM and PSM-based active damping.

In the following, the initial theoretical analysis, and the corresponding results, from [13] are further elaborated to discuss and illustrate the oscillatory behaviour that can appear in IPT systems with CVL and PDM. Simulation studies and experimental results are presented to validate the theoretical analysis while demonstrating the effectiveness and feasibility of the proposed methods for mitigating oscillations. An FPGA implementation of the PSM-based active damping method is introduced to minimize delays and improve the damping performance in comparison to the initial results presented in [13]. The results show that the proposed method for avoiding oscillations in CVL systems has negligible influence on the transient response to changes in the power reference, and that the transient use of PSM does not significantly reduce the efficiency of the system.

II. Models of IPT Systems with CVL and CRL

The topology of a typical SS-compensated IPT system is shown in Fig. 1, where v_1 (v_2), i_1 (i_2), L_1 (L_2), C_1 (C_2), and R_1 (R_2) are the sending (receiving) voltage, current, inductance, capacitance, and series-equivalent resistances, respectively, and M is the mutual inductance. A diode rectifier, connected to a battery modelled as a constant voltage load V_{dc_out}, is assumed at the pickup side to reduce system cost and complexity.

Based on the first harmonic approximation, the equivalent circuit of the SS-compensated IPT system is shown in Fig. 2 [4]-[12], [22]. Generally, in previous literature, IPT systems are commonly modelled with an equivalent CRL as shown in Fig.2(a). In this case, all steady-state parameters of the system can be easily analyzed and calculated. However, with a CVL the pickup voltage v_2 will remain constant in amplitude ($|v_2|= 2\sqrt{2}V_{dc\_out}/\pi$), but with a phase angle determined by the load current i_2 [9]. The phase and amplitude of i_2, and thereby the phase of v_2, will then change when the sending voltage changes. Therefore, the equivalent CRL model can only be used in steady-state conditions, which is not suitable for analyzing the dynamic characteristics, including the frequency response, or for controller design.

In order to further analyze the differences between CVL and CRL models, their state-space models and small-signal characteristics are discussed and compared. Assuming a synchronous reference frame dq representation of the state variables in a first harmonic approximation, the models can be derived and expressed in the general state-space form as [9]:

$$\begin{cases} \dot{\boldsymbol{x}} = f(\boldsymbol{x},\boldsymbol{u}) \\ \boldsymbol{y} = g(\boldsymbol{x},\boldsymbol{u}) \end{cases} \tag{1}$$

$$\boldsymbol{x} = [i_{1d} \quad i_{1q} \quad i_{2d} \quad i_{2q} \quad v_{C1d} \quad v_{C1q} \quad v_{C2d} \quad v_{C2q}]^T$$

$$\text{with } \boldsymbol{u} = \begin{cases} [v_{1d} \quad v_{1q} \quad \omega \quad V_{dc-out}]^T & CVL \\ [v_{1d} \quad v_{1q} \quad \omega \quad R_{eq}]^T & CRL \end{cases}$$

$$\boldsymbol{y} = [i_1 \quad P_{out}]^T$$

The resulting nonlinear state-space model of the SS-IPT system from Fig. 2 is expressed by the following 8 equations:

$$1)\ \frac{di_{1,d}}{dt} = \omega \cdot i_{1,q} - \frac{R_1}{L_{\alpha1}} \cdot i_{1,d} - \frac{MR_2}{L_{\alpha1}L_2} \cdot i_{2,d} - \frac{1}{L_{\alpha1}} \cdot v_{C1,d} - \frac{M}{L_{\alpha1}L_2} \cdot v_{C2,d} + \frac{1}{L_{\alpha1}} \cdot v_{1,d} - \frac{M}{L_{\alpha1}L_2} \cdot v_{2,d}$$

$$2)\ \frac{di_{1,q}}{dt} = -\omega \cdot i_{1,d} - \frac{R_1}{L_{\alpha1}} \cdot i_{1,q} - \frac{MR_2}{L_{\alpha1}L_2} \cdot i_{2,q} - \frac{1}{L_{\alpha1}} \cdot v_{C1,q} - \frac{M}{L_{\alpha1}L_2} \cdot v_{C2,q} + \frac{1}{L_{\alpha1}} \cdot v_{1,q} - \frac{M}{L_{\alpha1}L_2} \cdot v_{2,q}$$

$$3)\ \frac{di_{2,d}}{dt} = -\omega \cdot i_{2,q} - \frac{MR_1}{L_{\alpha2}L_1} \cdot i_{1,d} - \frac{R_2}{L_{\alpha2}} \cdot i_{2,d} - \frac{M}{L_{\alpha2}L_1} \cdot v_{C1,d} - \frac{1}{L_{\alpha2}} \cdot v_{C2,d} + \frac{M}{L_{\alpha2}L_1} \cdot v_{1,d} - \frac{1}{L_{\alpha2}} \cdot v_{2,d}$$

$$4)\ \frac{di_{2,q}}{dt} = -\omega \cdot i_{2,d} - \frac{MR_1}{L_{\alpha2}L_1} \cdot i_{1,q} - \frac{R_2}{L_{\alpha2}} \cdot i_{2,q} - \frac{M}{L_{\alpha2}L_1} \cdot v_{C1,q} - \frac{1}{L_{\alpha2}} \cdot v_{C2,q} + \frac{M}{L_{\alpha2}L_1} \cdot v_{1,q} - \frac{1}{L_{\alpha2}} \cdot v_{2,q}$$

$$5)\ \frac{dv_{c1,d}}{dt} = \omega \cdot v_{c1,q} - \frac{1}{C_1} \cdot i_{1,d} \quad 6)\ \frac{dv_{c1,q}}{dt} = -\omega \cdot v_{c1,d} + \frac{1}{C_1} \cdot i_{1,q}$$

$$7)\ \frac{dv_{c2,d}}{dt} = \omega \cdot v_{c2,q} + \frac{1}{C_2} \cdot i_{2,d} \quad 8)\ \frac{dv_{c2,q}}{dt} = -\omega \cdot v_{c2,d} + \frac{1}{C_2} \cdot i_{2,q} \tag{2}$$

where $L_{\alpha1}=L_1-M^2/L_2$, and $L_{\alpha2}=L_2-M^2/L_1$. It is worth noting that the expression of v_{2d} and v_{2q} shown in (2) are different for

Author Accepted Manuscript version of the paper by Zhou, J; Guidi, G; Ljøkelsøy, K and Suul, JA.
in IEEE Transactions on Power Electronics, Vol 38 (2023) Page 10412-10425, DOI: http://dx.doi.org/10.1109/TPEL.2023.3269698.

TABLE I
PARAMETERS OF SIMULATED IPT-SYSTEM

General parameters	Values
Nominal power, P_0	240 W
Input DC voltage, V_{dc_in}	40 V
Output DC voltage (CVL), V_{dc_out}	40 V
Output resistance load (CRL), R_{eq}	5.6 Ω
Nominal coupling	0.23
sending coil resonant frequency, f_{r1}	138.5 *kHz*
pickup coil resonant frequency, f_{r2}	140.0 *kHz*
Self-inductance, L_1, L_2	30.63, 30.48 μH
Quality factor, Q_1, Q_2	510, 490
Semiconductor devices (H-bridge and rectifier)	IRFS4010

the CVL and CRL models due to their load characteristics on the receiving side, as given by (3).

$$v_{2,dq} = \begin{cases} \dfrac{i_{2,dq}}{\sqrt{i_{2,d}^2 + i_{2,q}^2}} \cdot \dfrac{4}{\pi} \cdot V_{dc,out} & CVL \\ i_{2,dq} \cdot R_{eq} & CRL \end{cases} \tag{3}$$

For a fair comparison of results from these two cases, the steady-state points of the CRL model at resonance should be equivalent to the CVL model. The discussed system is nearly symmetrical as shown in Table I, so the maximum system efficiency can be achieved when V_{dc_out} is set to be the same as the input voltage. Correspondingly, R_{eq} in equation (3) can be calculated as [22]:

$$R_{eq}\Big|_{\omega=\omega_0} = \omega_0 \cdot k \cdot L_2 \tag{4}$$

where k is the coupling coefficient, expressed as $k = \dfrac{M}{\sqrt{L_1 \cdot L_2}}$.

For analyzing the small-signal dynamics of the state-space model, the system must be linearized at a steady state operating point defined by $f(\boldsymbol{x_0},\boldsymbol{u_0}) = 0$. Then, the small-signal model around the operating point $(\boldsymbol{x_0},\boldsymbol{u_0})$ is defined as:

$$\begin{cases} \Delta\dot{\boldsymbol{x}} = \mathbf{A}(\boldsymbol{x}_0, \boldsymbol{u}_0)\Delta\boldsymbol{x} + \mathbf{B}(\boldsymbol{x}_0, \boldsymbol{u}_0)\Delta\boldsymbol{u} \\ \Delta\boldsymbol{y} = \mathbf{C}(\boldsymbol{x}_0, \boldsymbol{u}_0)\Delta\boldsymbol{x} \end{cases} \tag{5}$$

The Jacobian matrices **A**, **B**, and **C** can be easily obtained by differentiating equations (2), as documented in [9], [13]. Based on the linear model in (5), the transfer function from the inputs to the outputs can be obtained as:

$$H(s) = \boldsymbol{C}(s\boldsymbol{I} - \boldsymbol{A})^{-1}\boldsymbol{B} \tag{6}$$

The Bode plots of the open-loop transfer functions from sending voltage to sending current for the CVL and CRL systems operated with nominal coupling at the resonant frequency are shown in Fig. 3 by using the parameters in Table I. It is worth noting that the pickup coil resonant frequency is designed to be slightly higher than the sending coil resonant frequency. This gives close-to-ideal zero voltage switching (ZVS) in a wide operating range [22]-[24]. The results in Fig.3 show that the Bode plot of the CVL model has a sub-resonant peak with a high amplitude, which can significantly influence the sending current when excited. The pickup current and output power of the IPT system with CVL will be determined by the sending current, and will, therefore,

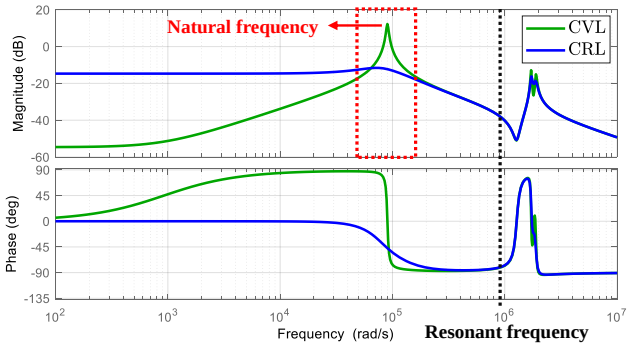

Fig. 3. Bode plot of open loop transfer function from v_1 to i_1 for the CVL and CRL models operated at nominal coupling and resonant frequency.

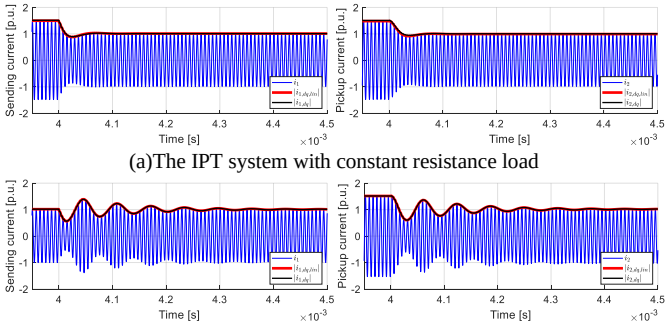

(a)The IPT system with constant resistance load

(b)The IPT system with constant voltage load

Fig. 4. A step change in the sending voltage from $0.5v_1$ to v_1.

experience similar oscillations. The natural frequency of the peak in the amplitude is about one-tenth of the resonant frequency when using the parameters in Table I. To further confirm the above analysis, simulation results for a sudden change in the sending voltage from 0.5p.u. to 1p.u. at t=4ms under the two different models are shown in Fig. 4. The blue lines represent the instantaneous current waveforms, while the black and red lines represent the amplitude of the instantaneous currents as obtained from the nonlinear state-space model from (5) and the corresponding linearized model, respectively. It can be seen from Fig.4 that the nonlinear and linearized state-space models can accurately capture the dynamic response of the system. Moreover, the IPT system with CRL has no oscillations in the current amplitude or the power and quickly reaches a steady state, while the IPT system with CVL will have a long period of current/power oscillations. Thus, it should be expected that IPT systems with CVL and CRL will behave differently when using pulse skipping modulation strategies such as PDM.

III. IPT SYSTEMS WITH CVL AND CRL UNDER (E)PDM

In PSM, the pickup voltage is regulated by controlling the Phase Shift Angle (PSA) of the H-bridge as shown in Fig. 5 (a), causing switching at non-zero current. However, PDM has recently been widely studied for ensuring soft switching at resonance to maintain high efficiency of IPT systems in a wide voltage range [14]. With PDM some of the pulses are removed in a whole switching cycle and hard switching is avoided, as illustrated in Fig. 5 (b). The ratio of the number of remaining pulses to the number of switching cycles is called

Author Accepted Manuscript version of the paper by Zhou, J; Guidi, G; Ljøkelsøy, K and Suul, JA.
in IEEE Transactions on Power Electronics, Vol 38 (2023) Page 10412-10425, DOI: http://dx.doi.org/10.1109/TPEL.2023.3269698.

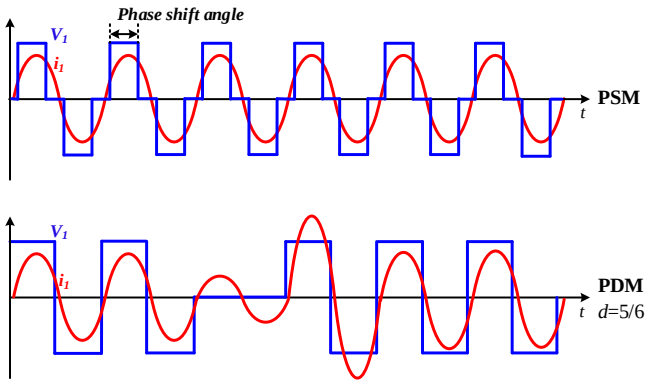

Fig. 5. Operating waveforms of IPT systems with PSM and PDM

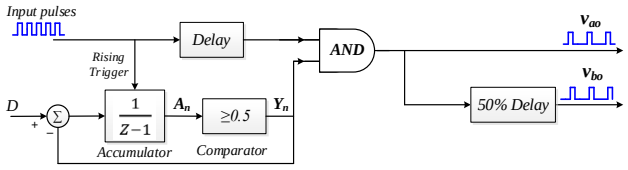

Fig. 6. Logics of the DSM-based PDM for a H-bridge converter.

pulse density, denoted by D. In this case, the average RMS fundamental components of v_1 over time can be calculated as $V_1 = 2\sqrt{2}\cdot D\cdot V_{dc\_in}/\pi$. Therefore, the average output power of IPT systems with PDM can be regulated by adjusting D, while avoiding the disadvantages of increased switching losses caused by loss of ZVS during voltage control by PSM.

Conventional PDM was first used in voltage-source inverters with a series resonant circuit and has later been widely adopted in IPT systems [15]. However, the conventional PDM selects a fixed pattern in a Read Only Memory (ROM) to control the output power/voltage, resulting in low density resolution [15], [16]. To obtain a uniformly distributed PDM pulse sequence with continuously varying pulse density, the delta-sigma modulator (DSM) can be used. The implementation of DSM-based PDM for half-bridge converters was presented in [14]. Based on the same principle, the DSM-based PDM for H-bridges can be easily obtained, as shown in Fig. 6. The core of the DSM-based PDM is an accumulator, which is triggered by the rising edges of the input pulse and accumulates the difference between pulse density D and the output of a comparator. The output of the comparator is combined with the delayed input pulses by an AND gate, whose output is the modulated output pulses.

Since the operating principle of PDM is to switch the sending voltage between 0 and the rated value, the resulting perturbation will always interfere with the steady-state operation and affect the system performance. In this paper, the performance of IPT systems with PDM under CVL conditions is studied and compared with the results under CRL conditions. Fig. 7 shows the sending voltage and sending current waveforms of IPT systems with CVL and CRL by implementing DSM-based PDM and using the parameters in Table I. Compared with the CRL model, the sending current oscillation of the IPT system with CVL is large, which results

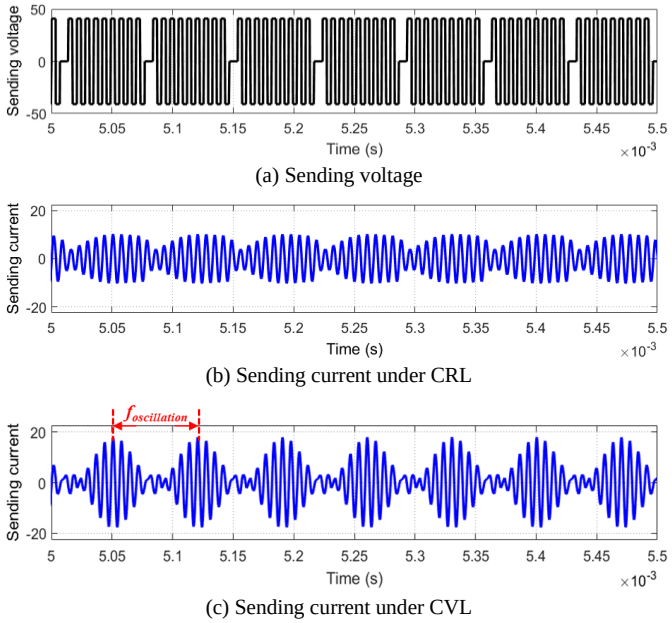

Fig. 7. IPT systems under PDM with D=0.9.

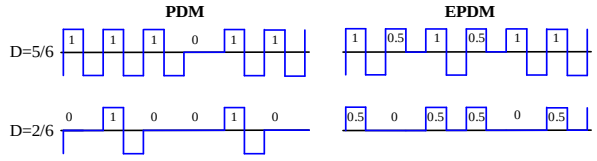

Fig. 8. Comparison between PDM and EPDM patterns for different densities.

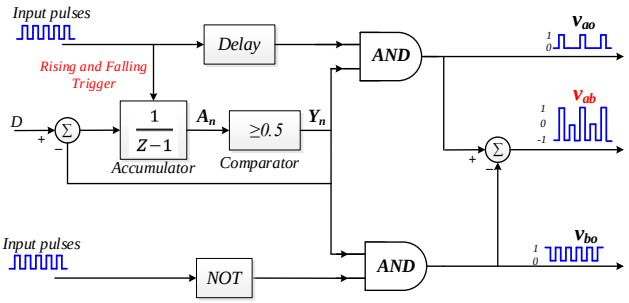

Fig. 9. Logics of the EPDM based on DSM for a full-bridge converter.

in high current stress of components, high voltage stress of resonant capacitors, and high output power oscillation. The oscillation frequency of the sending/pickup current amplitude is about 90000rad/s, which is consistent with the natural frequency identified in Fig. 3. In this case, when the frequency of the missing pulse of PDM is close to the natural frequency of the system (that is, D≈0.9), the oscillation of the system is the worst due to the continuous pulsation superimposed in phase with the triggered oscillations.

To limit the system oscillations caused by PDM, the commonly studied approach is to reduce the excitation of the critical oscillation frequency. For instance, in previous literature discussing resonant converters with CRL, an EPDM method based on the conventional PDM has been proposed to reduce the current ripple [25]. Different from the PDM according to Fig.5 and Fig. 6, the RMS of the sending voltage

Author Accepted Manuscript version of the paper by Zhou, J; Guidi, G; Ljøkelsøy, K and Suul, JA.
in IEEE Transactions on Power Electronics, Vol 38 (2023) Page 10412-10425, DOI: http://dx.doi.org/10.1109/TPEL.2023.3269698.

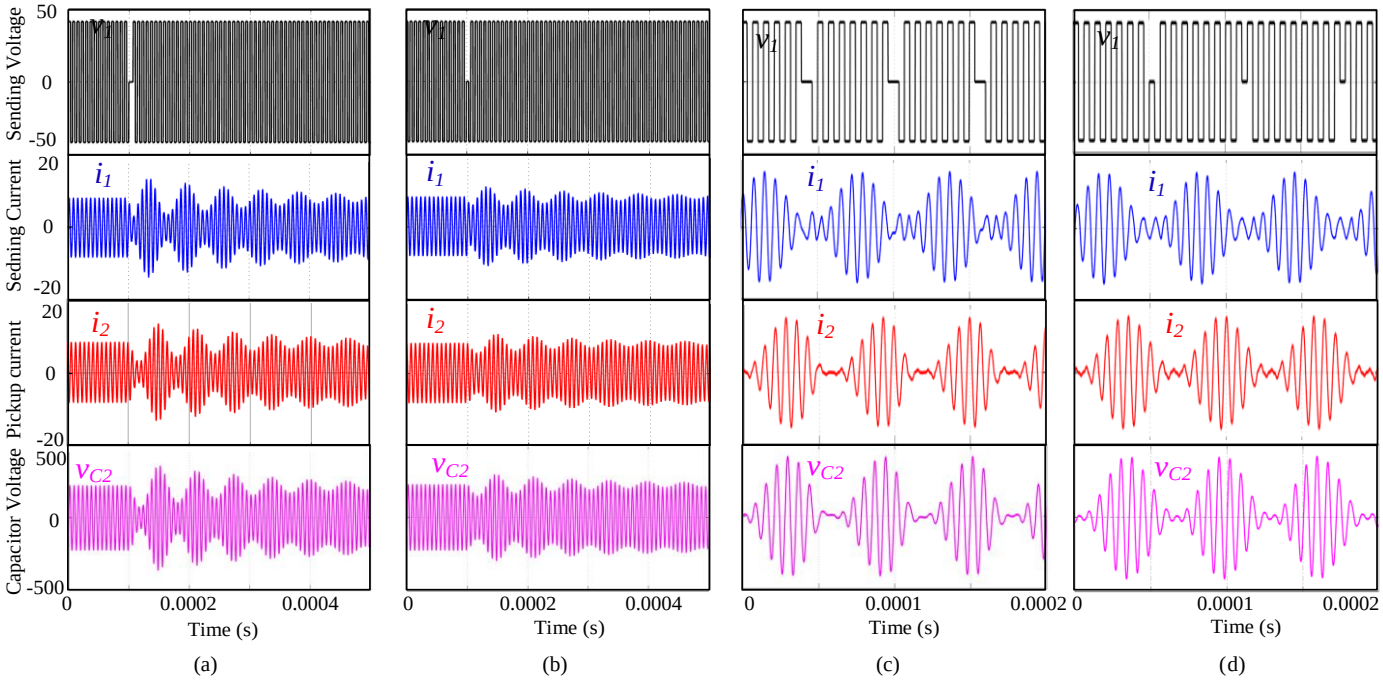

Fig. 10. The simulation results of the IPT system with PDM and EPDM. (a) implemented PDM with only one pulse missing; (b) implemented EPDM with only one pulse missing; (c) implemented PDM with the worst density (ΔI_{send}=93.75%); (d) implemented EPDM with the worst density (ΔI_{send}=93.75%).

in EPDM is switched between 0.5 V_1 and V_1, as shown in Fig. 8, which results in smaller current ripples. In this paper, EPDM is implemented based on DSM, as shown in Fig. 9. Thus, the accumulator of DSM-EPDM is triggered on both rising edges and falling edges of the input pulses, and the EPDM skips half periods of the input pulses instead of one full period. In this case, EPDM avoids simultaneous voltage changes of v_{ao} and v_{bo} in adjacent periods. Moreover, the change in the RMS of the output voltage is only half compared to PDM, and this will reduce the amplitude of the perturbation that excites the poorly damped oscillation mode of the CVL.

A comparison of results when the IPT system is operated with PDM and EPDM is shown in Fig. 10, based on simulations performed in Matlab/Simulink with the parameters from Table I. When only one pulse is missing according to PDM and EPDM patterns, the sending voltage, sending current, pickup current and receiving side resonant capacitor voltage v_{C2} of the IPT system are shown in Fig. 10 (a) and (b). The results demonstrate that the current oscillations of the IPT system with EPDM are much smaller than for the IPT system with PDM. This also verifies that EPDM usually causes lower current ripples due to a smaller perturbation in the sending voltage. Moreover, Fig. 10 (c) and (d) show the results of the IPT system using PDM and EPDM at the worst D, that is when the frequency of the missing pulse of (E)PDM is the same as the frequency of the current oscillation. Because of the superposition of oscillation currents with the same phase, EPDM behaves as badly as PDM, and the peak sending current values of both cases are around 15.6 A. In this case, the sending current ripples ΔI_{1_ripple}, defined as the percentage increase from the rated current value to the peak current value, are 93.75%.

Compared with the system using PDM, the IPT system with EPDM usually performs better, but as demonstrated, there can also be large current oscillation at certain densities due to low damping. Therefore, additional measures are needed to suppress current ripples also when EPDM is used in the IPT system with CVL. However, the skipping pulses of the system with PDM are frequent and are not given by any simple analytical expression, which greatly increases the difficulty of analyzing the original 8th-order system. Indeed, the DSM-based (E)PDM can generate continuous density but the dependency on the initial conditions imply that no explicit analytical solutions exist for calculating the timed-domain response or the resulting current oscillations of the system. In this case, general methods are needed to suppress the ripples in any combination of missing pulses, rather than for specific patterns of skipped pulses in conventional PDM.

IV. Methods for Eliminating Oscillation by Increasing System Damping

In this section, two approaches for increasing the damping of IPT systems with CVL by control are studied. First the operation at off-resonance frequency is analysed, before the active damping of the oscillations by additional feedback control according to [13] is further investigated. It is worth noting that these methods can be applied in combination with any PDM implementation, but DSM-based EPDM will be assumed in the following to minimize the perturbations in the input voltage.

Author Accepted Manuscript version of the paper by Zhou, J; Guidi, G; Ljøkelsøy, K and Suul, JA.
in IEEE Transactions on Power Electronics, Vol 38 (2023) Page 10412-10425, DOI: http://dx.doi.org/10.1109/TPEL.2023.3269698.

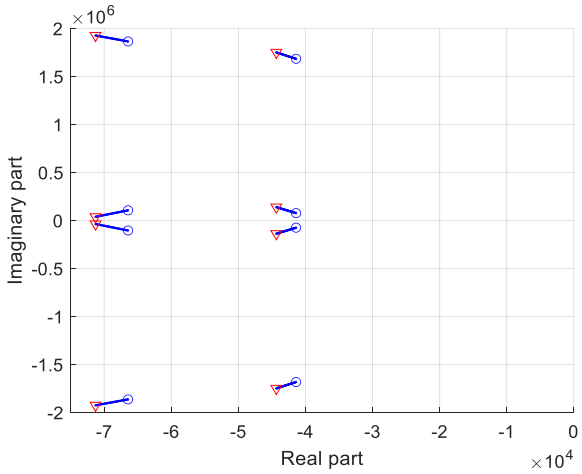

(a) CRL system

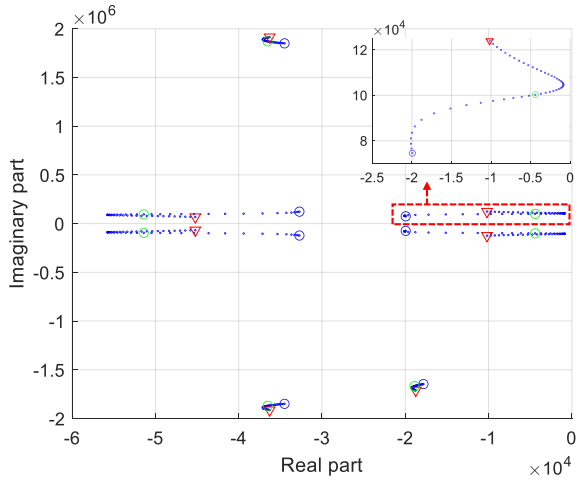

(b) CVL system

Fig. 11. Eigenvalue trajectory for variation of frequency in the range of 0.975 f_0 < f < 1.05 f_0: points marked with blue circles, green circles, and red triangles are corresponding to f=0.975f_0, f=1.0f_0, and f=1.05f_0, respectively.

A. Operation with Slightly Off-resonant Frequency for Increasing Damping

IPT systems with CRL and well-damped characteristics are usually operated at the resonant frequency to achieve optimal efficiency during voltage control [14], [26]. However, as demonstrated, CVL systems can have a very low damping at the critical frequency, which can easily cause system oscillations. Since the damping of the critical oscillation mode can be influenced by the operating frequency, the impact of off-resonant operation is discussed in the following by weighing the system response and efficiency.

To achieve ZVS over the whole frequency range of interest for power regulation, both CRL systems and CVL systems can be designed with a detuning factor x_c (x_c = $C_1 \cdot L_1/(C_2 \cdot L_2)$) slightly greater than 1 to ensure an inductive sending side impedance [22], [24]. In the following discussion, x_c is kept at 1.05 and f_0 is the resonant frequency of the pickup side. Based on analysis of the small-signal model from (5), Fig. 11 shows the eigenvalue trajectory of the ***A***-matrix for CVL systems and CRL systems when the operating frequency is changed from 0.975f_0 to 1.05f_0. In the figures, points marked with blue circles, green circles, and red triangles are corresponding to f=0.975f_0, f=1.0f_0, and f=1.05f_0, respectively.

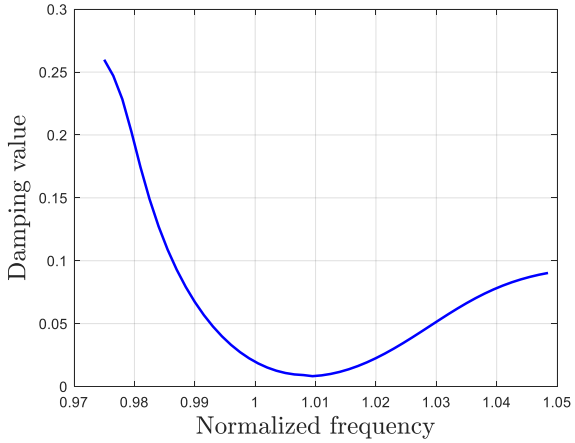

Fig. 12. The damping value of the IPT system with CVL at different operating frequencies.

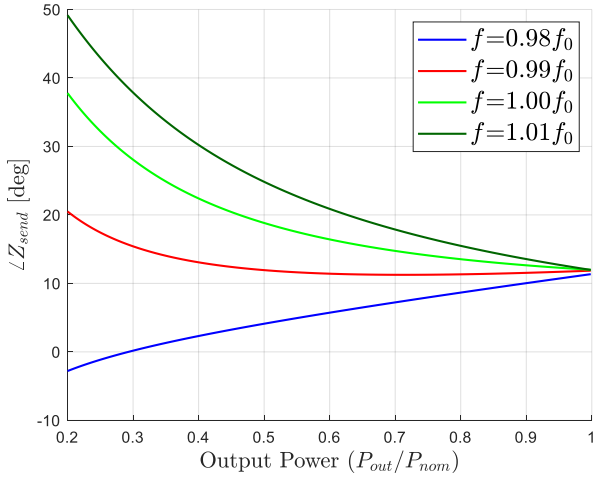

Fig. 13. The input impedance angle of the IPT system with CVL at different operating frequencies.

As seen from Fig. 11(a), the dominant pole-pair of the CRL system is always far from the imaginary axis, confirming that the system has a good damping value (ζ=0.47 at the resonant frequency) and short settling time. Moreover, the change of the operating frequency has little effect on the eigenvalues and the corresponding damping. Therefore, IPT systems with CRL characteristics can operate at the resonant frequency to obtain optimal efficiency [14]. However, the eigenvalue trajectory of the CVL system is more complicated, as shown in Fig. 11(b). As the operating frequency moves away from the resonance frequency, the ratio of the real part to the imaginary part increases rapidly, resulting in a gradual increase in system damping. The corresponding damping coefficient of the critical mode at different operating frequencies is plotted in Fig. 12, which shows how the damping of the system is very low near the resonant frequency. As the operating frequency moves away from the resonant frequency, the system damping increases rapidly, and the rising slope is steeper in the sub-resonant region. The damping at off-resonant frequencies (for instance ζ=0.2598 at

Author Accepted Manuscript version of the paper by Zhou, J; Guidi, G; Ljøkelsøy, K and Suul, JA.
in IEEE Transactions on Power Electronics, Vol 38 (2023) Page 10412-10425, DOI: http://dx.doi.org/10.1109/TPEL.2023.3269698.

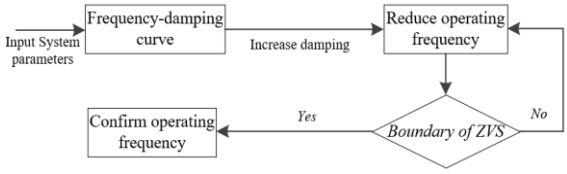

Fig.14. The selection process of the operating frequency.

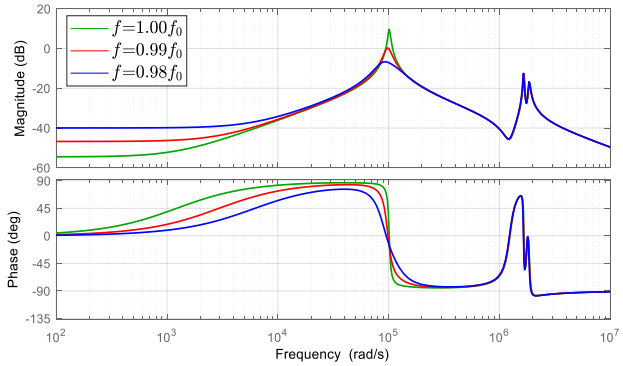

Fig. 15. Bode plot of the transfer function from v_1 to i_1 for the CVL model with different operating frequencies.

f=0.975f_0 and ζ=0.0903 at f=1.05f_0) can be much higher than that at the resonant frequency (ζ=0.018), and the IPT system operated at sub-resonant frequency performs best for the dynamic response. Theoretically, the system damping will further increase if the operating frequency is decreased beyond the values shown in Fig. 12. However, the selection of operating frequency during voltage control should not only consider the system damping, but also the system efficiency. Especially, ZVS needs to be ensured to maintain high system efficiency in the full operating range.

Based on the nonlinear model shown in (2), all the steady-state parameters of the system can be solved. Thus, the input impedance angle of the system with CVL for voltage control at different operating frequencies can be calculated as a function of the power transfer, resulting in the curves shown in Fig. 13. The curves show how the system can always achieve ZVS at rated power. However, when the operating frequency of the system is 0.98f_0, the input impedance of the system becomes capacitive as the output power decreases, causing the system to lose ZVS under light load conditions.

To ensure high efficiency over the full operating range, the operating frequency should be as low as possible for providing high damping while still ensuring ZVS. The applied process for selecting the operating frequency is shown in Fig. 14. In this case, the operating frequency is selected as 0.99f_0 to achieve ZVS in the full operating range. If the system is not required to work under light loads such as 0.3 P_{nom}, the operating frequency can be selected as 0.98f_0. Finally, the frequency response of the IPT system with CVL at f_0, 0.99f_0 and 0.98f_0 is shown in Fig. 15. As expected, the peak of the amplitude response is reduced as the operating frequency decreases, which implies that the system remains reasonably well-damped at the slightly sub-resonant frequency.

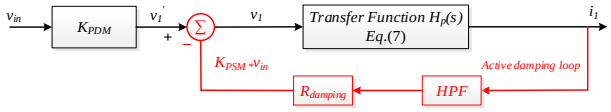

Fig. 16. The control block of active damping methods based on sending current feedback and PSM.

B. *Active Damping Control*

Although the oscillations in IPT systems with CVL characteristics can be reduced by EPDM and sub-resonant frequency operation, there can still be large oscillations at some specific values of D. The main reason is that CVL IPT systems with high efficiency naturally have a very low damping value at the critical oscillation frequency. As for the damping of LCL filters in grid-connected converters [27], [28], a simple way to eliminate current oscillations is to add a virtual/real resistance in the circuit loop to achieve active/passive damping. However, adding a real resistance to the main circuit of IPT systems will greatly increase the conduction losses. Therefore, only active damping methods are considered.

For the IPT system with CVL and (E)PDM, frequent changes in the sending voltage cause the oscillation of the sending current, which further results in large ripples in the pickup current and output power. Therefore, the suppression of the sending current oscillation is the primary task. Fig. 16 shows the control block diagram of the active damping method based on sending current feedback, as proposed in [13]. In the figure, the black part is the original model, which includes the H-bridge using PDM and the transfer function of the plant under study. According to the small-signal model shown by equations (5) and (6), the corresponding 8th-order transfer function from sending voltage to sending current can be obtained as:

$$H_p(s) = \left[\boldsymbol{C}(s\boldsymbol{I}-\boldsymbol{A})^{-1}\boldsymbol{B}\right]_{1,3} \tag{7}$$

where the subscripts (1,3) represent the elements of the first row and third column of the matrix. Moreover, an active damping loop using virtual resistance could be added to the original model, as highlighted in red. Since the damping should only work on the current ripple, a high-pass filter (HPF) is introduced in the controller to remove the DC component of the sending current amplitude. The transfer function of HPF is

$$H_f(s) = \frac{T_f s}{1+T_f s} \tag{8}$$

where T_f is the time constant, and its value is 100/(2*π*f_0). In this case, the cutoff frequency of the HPF is 1/100 of the resonant frequency. When considering the system discussed in Table 1, the natural frequency of the system is typically 1/10 of the resonant frequency as shown in Fig. 3. As coupling increases, so does the natural frequency of the system. When the operating coupling is reduced to half of the rated value, the system's natural frequency changes to approximately 1/17 of the switching frequency. Therefore, the components of the

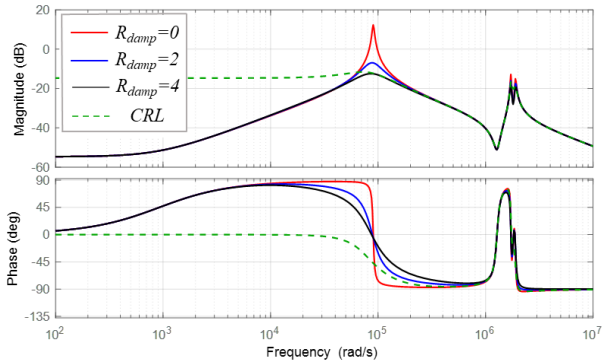

Fig.17. Bode plot of the transfer function from v_1 to i_1 for the CVL model with active damping methods.

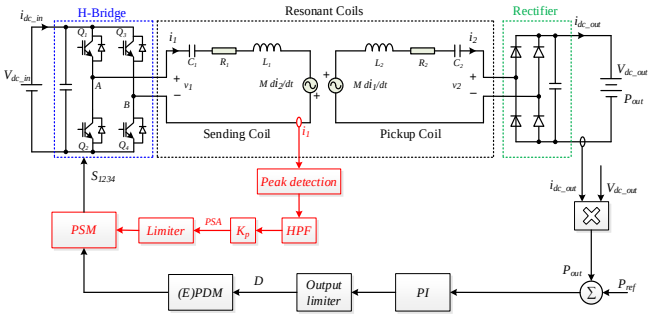

Fig. 18. The proposed control strategy of the IPT system with CVL under PDM.

system are hardly affected by the designed HPF. Then the closed-loop function of the system can be obtained as:

$$G(s)=\frac{H_p(s)}{1+R_{damp}\cdot H_p(s)\cdot H_f(s)} \tag{9}$$

It is worth noting the PDM needs multiple cycles to reflect the average *D*, which prevents the effective implementation of damping methods acting on the input voltage reference. Instead, the active damping is implemented by a feedback loop introducing PSM on the voltage pulses generated by the PDM. This ensures a fast response by acting on the voltage within each switching period [13]. The resulting frequency response of the system with different values of the virtual resistance is shown in Fig. 17. It can be found that the sub-resonant peak at the natural frequency point decreases significantly with the increase of the virtual resistance. Moreover, the frequency response of the CRL system with the same equivalent load is shown in the figure by green dashed lines. The CRL system has a damping coefficient of 0.47, which ensures good performance even in the worst case, as was shown in Fig. 7. Therefore, the virtual impedance of the CVL system can be designed to have a natural frequency peak similar to that of the CRL system with a resistance value of 4 Ohm, as shown in Fig. 17. In this case, the feedback voltage value ΔU_1 of the system can be calculated as:

$$\Delta U_1 = R_{damp}\cdot\Delta I_1 \tag{10}$$

where ΔI_1 is the ripple of the sending current amplitude.

The resulting overall control strategy when including active damping with PSM is shown in Fig. 18. Starting from the original (E)PDM, a sending current feedback control loop with PSM is added. The amplitude of the sending current is measured by a peak current detection algorithm. Although the signal conditioning for the peak current detection includes a low pass filter (LPF) for attenuating noise, the time constant is very small (T_{LPF}=10^{-7}s) and hardly affects the active damping control. The high crossover frequency of the LPF also ensures that it does not interfere with the detection of the oscillating component by the HPF. This isolated ripple component of the sending current is used as input to a proportional controller k_p which provides a PSA and then performs PSM on the pulses resulting from the PDM. Thus, the active damping method can be considered to apply a virtual resistance to the oscillating component of the sending side current feedback to suppress the current/power oscillations. The actual feedback voltage value ΔU_1 of the system is obtained as:

$$\Delta U_1 = \left[1-\sin\left(\frac{\pi-k_p\cdot\Delta I_1}{2}\right)\right]\cdot U_1 \tag{11}$$

Therefore, the proportional controller k_p can be calculated by combining equations (10) and (11):

$$k_p=\frac{1}{\Delta I_1}\left(\pi-2\arcsin\left(1-\frac{R_{damp}\cdot\Delta I_1}{U_1}\right)\right) \tag{12}$$

To avoid excessive current stress of the H-bridge, ΔI_1 is expected to be controlled within 25% of the rated current. Then k_p can be calculated as 0.68. Moreover, the operating range of PSA can also be roughly estimated:

$$\varphi \geq \pi - k_p\cdot\Delta I_{1\_\max} \tag{13}$$

In this case, the range of PSA is within 0.57π – π (102° – 180°), i.e. the sending voltage range is 0.78 – 1 U_1. It is worth highlighting that the HPF filtering eliminates low-frequency components from the sending current amplitude, preventing from the DC component from causing additional PSA output. Furthermore, the system only implements PSM transiently during a few cycles as needed to effectively eliminate the current ripples.

C. Simulation Results

In the previous subsections, two methods have been introduced for suppressing oscillations caused by CVL characteristics, and they can all be simultaneously implemented for IPT systems. Therefore, the final proposed control strategy is to apply the active damping method in the IPT system with DSM-based EPDM while operating the system at a slightly sub-resonant frequency. This can ensure high-density resolution, low current/power ripple, and high efficiency. The effectiveness of the proposed strategy will be first validated by simulation, while experimental results will be presented in a separate section.

Simulations have been performed with Matlab/Simulink by using the parameters provided in Table I. Fig. 19 (a)-(c)

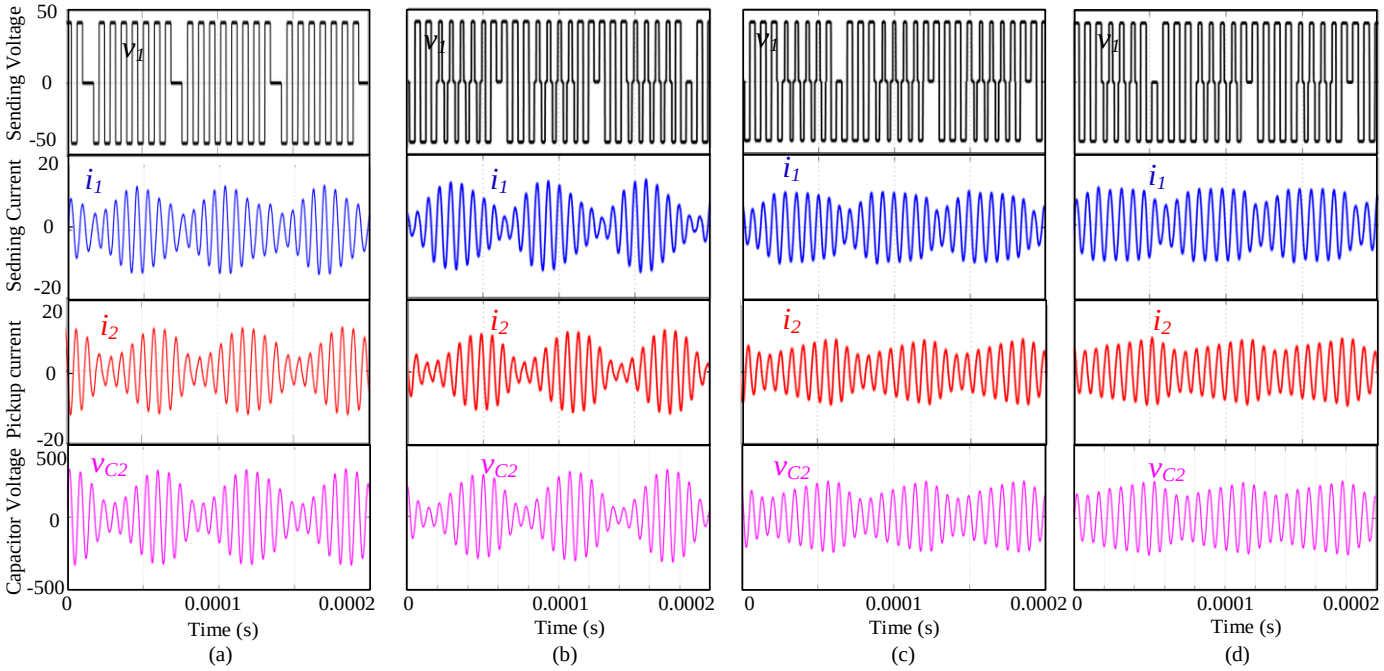

Fig. 19. The simulation results of the IPT system with proposed methods at the worst density. (a) off-resonance operation (ΔI_{1_ripple} =58.75%); (b) active damping method with PSA output limited between 126° and 180° (ΔI_{1_ripple}=56.25%); (c) active damping method with PSA output limited between 90° and 180° (ΔI_{1_ripple} =31.25%); (d) combining EPDM, off-resonance operation and active damping method with PSA output limited between 126°and 180° (ΔI_{1_ripple}=25%).

presents examples of waveforms from the IPT system when operated with the individual proposed methods at the worst *D*. The results of the IPT system operating at the off-resonance frequency (f=0.98f_0) are shown in Fig. 19 (a), where the current oscillation is greatly reduced compared to Fig. 10 (c) and (d), and the peak sending current value is 12.8 A. Similarly, the results of the IPT system with the active damping method are presented in Fig. 19 (b) and (c), where their output PSA are limited to 126°-180° and 90°-180°, respectively. As expected, the current oscillation is also suppressed, and the peak current value decreases as the minimum PSA reduces. However, a too-low minimum PSA causes the system to lose ZVS in many switching periods, giving high switching losses. Therefore, the PSA should be set as large as possible, and the PSM should work in as few cycles as possible. Finally, all the above methods that can suppress the current oscillation are combined, that is, applying PSM-based active damping in the IPT system with EPDM and off-resonant operation. The PSA is limited between 126° and 180° to ensure high efficiency. The corresponding simulation result is shown in Fig. 19 (d), where the current oscillation of the system is significantly suppressed. The peak sending current value is 9.4A. Thus the sending current ripples of the system are reduced from 7.7A to 1.5A. For this case, the system implements high-PSA PSM for approximately 2/5 periods. Therefore, the above results validate the effectiveness of the proposed strategy.

D. Evaluation on Presented Methods

To evaluate the proposed method in detail, the system performance will be comprehensively evaluated in this section. First, the losses of the system under different working conditions are analyzed in detail. For this purpose, the averaged losses of the system with PDM are analyzed based on the natural oscillation period (T_p) and expressed as:

$$P_{loss}=\frac{1}{T_p}\int_{-\frac{T_p}{2}}^{\frac{T_p}{2}}\Big(I_1^2(t)R_1+I_2^2(t)R_2+2I_1^2(t)R_{\text{Mos-on}}+2I_2^2(t)R_{diod\text{-}on}+\frac{4\sqrt{2}}{\pi}V_T I_2(t)+2\sqrt{2}V_{ds}I_1(t)\sin(\theta)\cdot\left(\frac{e_{SW\_OFF}}{V_R I_R}\right)\cdot f_o\Big)dt \tag{14}$$

where $I_1(t)$ and $I_2(t)$ are the sending current and pickup current amplitudes of the system with PDM, respectively; $R_{Mos\text{-}on}$ is the equivalent on-state resistance of MOSFETs; θ is the phase shift between the sending voltage and the sending current; V_R and I_R are the rated drain-source voltage and source current of MOSFET; e_{SW_OFF} are the rated turn-off energy losses of MOSFET; f_o is the operating frequency; V_T and $R_{diod\text{-}on}$ are the threshold voltage and the equivalent on-state resistance of the rectifier diode, respectively.

Moreover, the losses of systems with PDM and active damping are discussed. To suppress ripple, a high-PSA PSM is introduced to the system for a few cycles, resulting in additional switching losses. However, these additional losses will be shown to have minimal effects on total losses. Neglecting small current fluctuations, the sending/pickup currents of the system with active damping can be assumed to be constant values, and the total losses of the presented system can be expressed as:

$$P_{loss}=\frac{I_1^2R_{H\text{-}diod\text{-}on}}{\pi}(\pi-\varphi-\sin\varphi)+\frac{2\sqrt{2}}{\pi}V_{H\text{-}T}I_1\left(1-\sin\frac{\varphi}{2}\right)$$
$$+\frac{1}{\pi}I_1^2R_{Mos\text{-}on}(\pi+\varphi+\sin\varphi)+2I_2^2R_{diod\text{-}on}+\frac{4\sqrt{2}}{\pi}V_TI_2$$
$$+2\sqrt{2}V_{ds}I_1\cos\left(\frac{\varphi}{2}\right)\cdot\left(\frac{e_{SW\_ON}+e_{SW\_OFF}}{V_RI_R}+\frac{Q_{RR}}{I_{R\_D}}\right)\cdot f_o \quad (15)$$

where $V_{H\text{-}T}$ and $R_{H\text{-}diod\text{-}on}$ are the threshold voltage and the equivalent on-state resistance of the body diode of MOSFETs of the H-bridge, respectively; e_{SW_ON} are the rated turn-on energy losses of MOSFET; Q_{RR} and I_{R_D} are the reverse recovery charge and the rated current of the body diode of the H-bridge.. It is worth noting that phase shift angle φ is π in most cycles, which does not cause additional switching losses.

For systems with DSM-PDM, the output patterns are too numerous to be analyzed one by one. In this case, the system operating at worst D is used as an example to calculate the losses of the system with PDM and active damping. Moreover, the time-domain expressions of the sending/pickup current cannot be analytically calculated due to the 8th-order system and uncertain initial conditions. In this case, the loss calculation can be performed by fitting a function according to the peak current of the simulation result shown as in Fig. 10(d). When the system with active damping operates at the worst D, the PSM is introduced in about 3 switching cycles in each oscillation period, and the corresponding PSA is about 0.72π, 0.57π and 0.72π shown in Fig. 19(d). Based on the parameters in Table I and Equations (14)-(15), the efficiency for operation without and with active damping at the worst D can be calculated as 96.3% and 96.6%, respectively. In this case, it is clear that the additional conduction losses caused by large oscillations in the sending/pickup currents are higher than the additional switching losses of the proposed PSM-based active damping introduced to attenuate these oscillations.

Table II. System Performance under Different Control Strategies

	Dynamic performance	Efficiency	Harmonic distortion
PSM	Good	Low	Low
PFM	-----	-----	Low
PDM	Average	High	High
PDM with active damping	Average	High	Average

Finally, a comprehensive comparison of the performance of systems with different control strategies is provided in Table II. Compared with the classic PSM, PDM can achieve full-range soft switching, thereby greatly improving the efficiency. Compared with PSM, PDM generally requires more switching cycles to implement pattern and power regulation due to ripples, resulting in a slightly slower dynamic response. Notably, the active damping loop has no impact on the power regulation of the system. However, the implementation of PDM requires a few more cycles. The IPT system with PDM without the proposed damping experiences significant sub-harmonic oscillations, which are effectively suppressed to be low by the presented method in this paper. For systems with pulse frequency modulation (PFM), the output harmonics are low and the efficiency can be kept high over a wide operating range [22]. However, the output power of the frequency-controlled system is limited, and it is difficult to ensure good dynamic performance due to nonlinear characteristics. Overall, IPT systems with the proposed methods can achieve high efficiency over the full operating range while maintaining low ripples and acceptable dynamic performance.

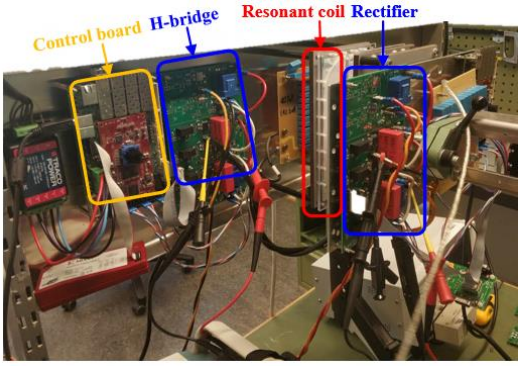

Fig. 20. Experimental setup of the IPT system.

V. Experimental Results

To further prove the results from the analysis and simulations, experiments are conducted with a laboratory prototype as shown in Fig. 20, designed with parameters listed in Table I [22]. In the experiments, the input/output DC voltages were set to 30 V to avoid excessively high current oscillations. Compared to the inial results presented in [13], an FPGA-implementation of the active damping has been developed to reduce the delays and improve the damping performance.

Fig. 21 shows the experimental results of the IPT system at the worst *D* under different methods. As expected, the IPT system with PDM has large sending/pickup current ripples, and the peak-to-peak sending current is about 20.9 A. In this case, the large current ripples lead to higher conduction losses, thereby reducing the system efficiency. Although the IPT system with EPDM usually performs better, it also has large current ripples at the worst *D*, as shown in Fig. 21(b). It is worth noting that the system efficiency in this case cannot be directly compared with the worst case of the IPT system with PDM, because the operating *D* is different. The oscilloscope plots reveal hard switching events by the overvoltage spikes they generate.

Fig.21(c) shows the results of the IPT system with PDM at a slightly sub-resonance frequency (f=0.98f_o). It can be found that the sending/pickup current ripples are effectively reduced, so the system efficiency is also greatly increased compared to the original system. The results of the IPT system with active damping based on PDM are shown in Fig.21 (d)-(e), when the PSA intervals are limited to 126°-180° and 90°-180°, respectively. Compared with the results of the initial IPT system with PDM, the current ripples of the system with the

Author Accepted Manuscript version of the paper by Zhou, J; Guidi, G; Ljøkelsøy, K and Suul, JA.
in IEEE Transactions on Power Electronics, Vol 38 (2023) Page 10412-10425, DOI: http://dx.doi.org/10.1109/TPEL.2023.3269698.

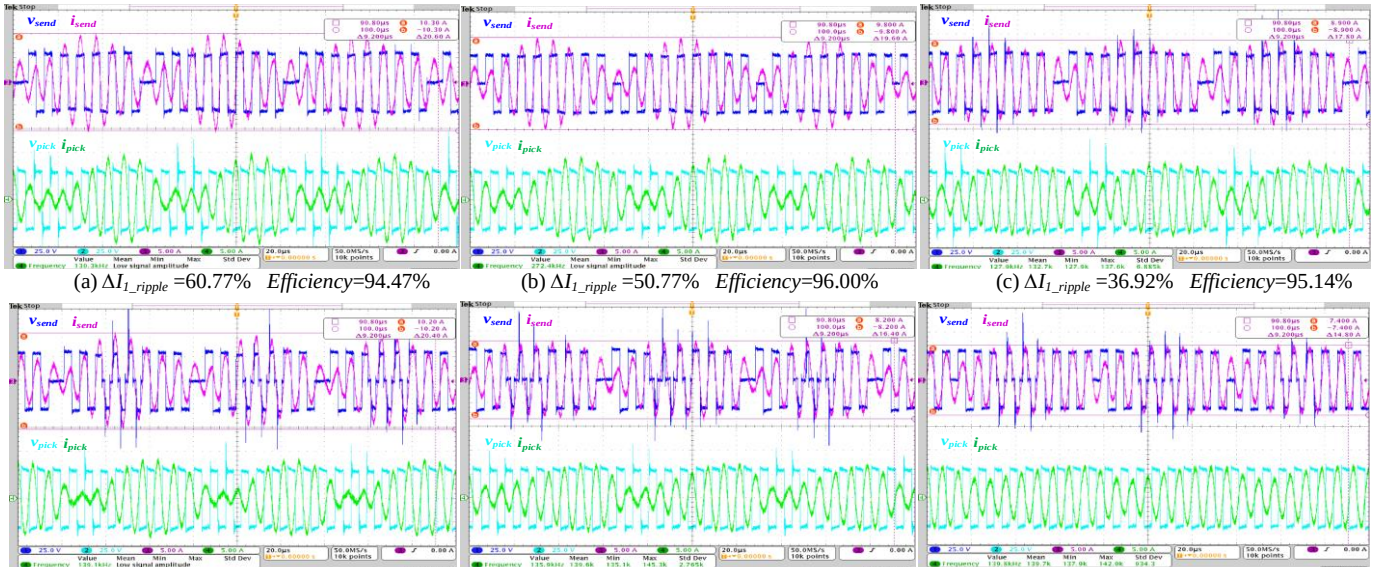

(a) ΔI_{1_ripple} =60.77% *Efficiency*=94.47% (b) ΔI_{1_ripple} =50.77% *Efficiency*=96.00% (c) ΔI_{1_ripple} =36.92% *Efficiency*=95.14%

(d) ΔI_{1_ripple} =56.92% *Efficiency*=95.12% (e) ΔI_{1_ripple} =26.15% *Efficiency*=95.02% (f) ΔI_{1_ripple} =13.85% *Efficiency*=96.23%

Fig. 21. The experimental results of the IPT system at the worst density. (a) PDM results (D=0.88); (b) EPDM results (D=0.94); (c) PDM results at f=0.98f_o; (d) PDM results with the active damping method (PSA∈[126°,180°]); (e) PDM results with the active damping method (PSA∈[90°,180°]); (f) EPDM results with the active damping method (PSA∈[126°,180°]).

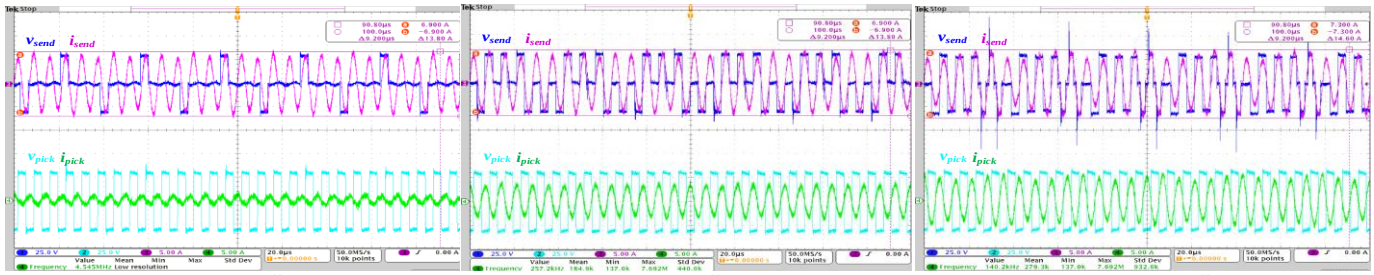

(a) ΔI_{1_ripple} =6.15% *Efficiency*=85.41% (b) ΔI_{1_ripple} =6.15% *Efficiency*=95.73% (c) ΔI_{1_ripple} =12.31% *Efficiency*=96.00%

Fig. 22. The experiment results of the IPT system with EPDM and the active damping method (PSA∈[126°,180°]). (a) D = 0.20; (b) D = 0.60; (c) D =0.90.

active damping method are correspondingly reduced, thus the system efficiency is increased. Moreover, the effect of suppressing current ripples is improved with decreasing minimum PSA, as shown in Fig. 21(d) and Fig. 21(e), but the efficiency is slightly reduced. Finally, the result of the IPT system with the active damping method based on EPDM is presented in Fig.21(f). The PSA in this case is limited between 126° and 180° for maintaining low switching losses. Compared with the peak-to-peak sending current of 19.6 A in the IPT system with EPDM, the value in the system with the active damping method is reduced to 14.8 A. Thus the sending current ripples are reduced from 4.42 A for the original system to 1.37 A with the proposed active damping control. It is worth noting that this result is lower than 1.57 A as achieved under similar conditions in [13], because the low latency in the damping system given by the FPGA implementation improves the damping performance. Moreover, it can be seen from Fig. 21(f) that the system implements high-PSA PSM for approximately 3/10 periods, which leads to losing ZVS in several cycles and increases the switching losses. However, the conduction loss of the system is reduced due to the lower current ripples. Therefore, compared with the 96.00% efficiency of the original EPDM system, the efficiency of the system under active damping is slightly increased to 96.23%.

From these results, it can be found that the system with EPDM and high-PSA active damping can perform well at the worst D, even without introducing sub-resonant operation. Furthermore, the x_c value in the prototype is low, so the sub-resonant operation can easily cause the system to lose ZVS under light load. Therefore, the sub-resonance operation is not introduced to increase damping in this case. However, the advantage of the sub-resonance operation would be more obvious in a system with sufficient inductive input impedance margin.

Additional results for the case with EPDM and active damping method are given in Fig.22. It can be found that the current ripples are always small. Moreover, high-PSA PSM is implemented in a few cycles, thus the system efficiency is close to that of the system with EPDM.

Considering the dynamic response of the system, Fig. 23 shows the normalized transferred power and sending current amplitude when the reference power changes from 50W to 100W at 0.05s in the system without/with active damping method based on EPDM. It can be found that the transferred

Author Accepted Manuscript version of the paper by Zhou, J; Guidi, G; Ljøkelsøy, K and Suul, JA.
in IEEE Transactions on Power Electronics, Vol 38 (2023) Page 10412-10425, DOI: http://dx.doi.org/10.1109/TPEL.2023.3269698.

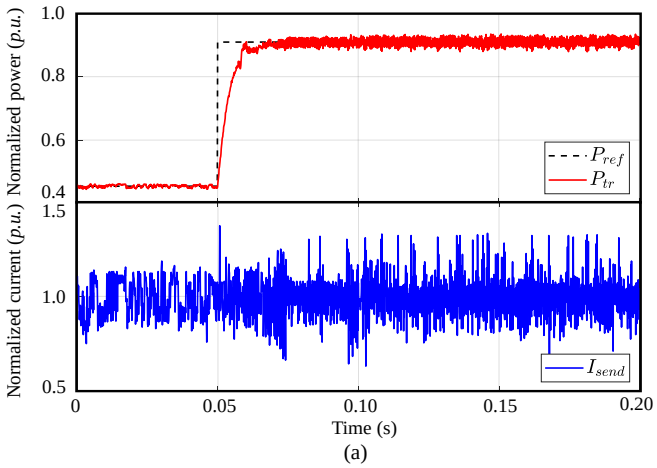

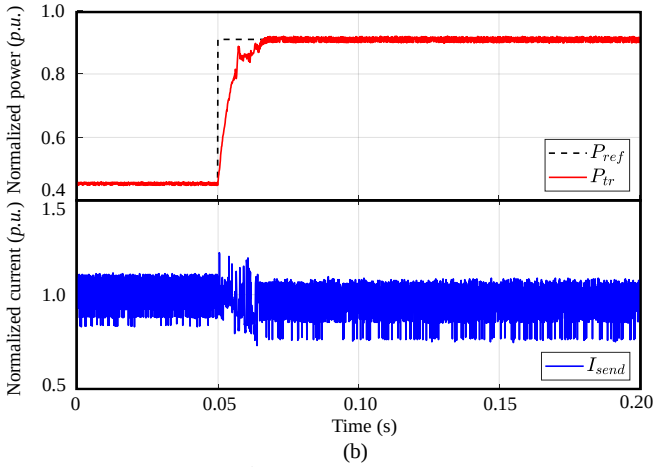

Fig. 23. Dynamic response of the IPT system with EPDM. (a) without actvie damping; (b) with actvie damping (PSA∈[126°,180°]).

power of the system in both cases can quickly track the reference power within 0.03s. Compared with the system without active damping, the transferred power of the system with active damping is smoother. More importantly, the maximum sending current amplitude of the undamped system is fluctuating in a wide range and is much larger than the rated current value, while the maximum current amplitude of the system with active damping is stable and only slightly higher than the rated current. Therefore, the system with active damping has a good dynamic response and can effectively suppress current/power ripples in any situation.

The sending current ripples of the IPT system with different methods under varying pulse densities are shown in Fig. 24. It can be found that the system with PDM has higher current ripples over the full operating range, especially at high modulation densities. Compared to the system with PDM, the system with EPDM performs better overall, but still performs poorly at high modulation densities. The sending current of the system with EPDM exceeds the rated value by 50% at the worst case, which means that the current stress on the power semiconductor and current/voltage stress on the resonant capacitors are significantly increased. The system with active damping control can significantly alleviate the above problems. It can be seen from Fig.24 that the current ripples

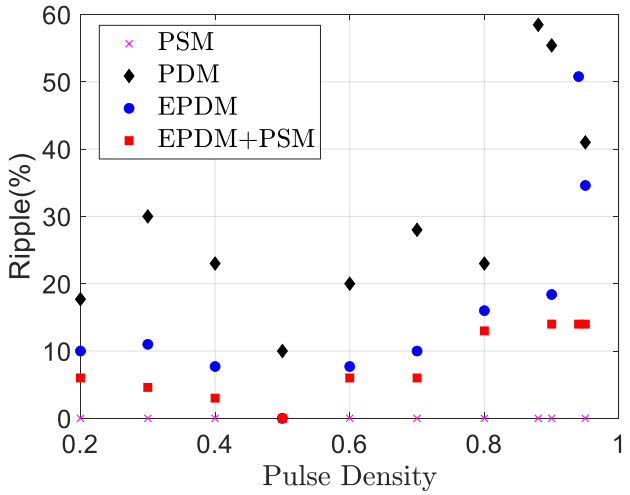

Fig. 24. The sending current ripples of the IPT system with different methods.

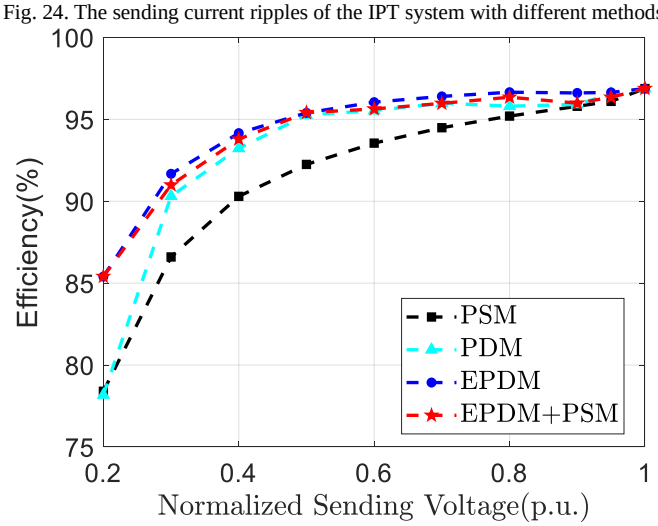

Fig. 25. The efficiency of the IPT system with different methods.

of the system with active damping control are always below 15% of the rated current, which greatly reduces the requirements for the current stress of the power semiconductor and reduces the output power ripples. In fact, operation with EPDM performs well in most cases, so PSM-based damping does not have to be activated for in all conditions, as shown in Fig. 22 (a) and (b). In the worst case of the system, high-PSA PSM is introduced for about 3/10 periods, which has little effect on the system efficiency, as shown in Fig.21 (f). The introduction of active damping control can reduce the maximum current stress of the power semiconductor by about 35% and ensure low output current/power ripples under any operating conditions, which is suitable for high-power applications.

The efficiency of the IPT system with different control methods under varying *D* is given in Fig.25. It can be found that the efficiency of the system with PDM/EPDM is much higher than that of conventional PSM, especially at light load. For the system with PDM, when *D* is very low, the pickup current is small. However, there is always a large ripple current in the system, which causes discontinuous pickup

Author Accepted Manuscript version of the paper by Zhou, J; Guidi, G; Ljøkelsøy, K and Suul, JA.
in IEEE Transactions on Power Electronics, Vol 38 (2023) Page 10412-10425, DOI: http://dx.doi.org/10.1109/TPEL.2023.3269698.

current, aggravates the current ripples and reduces the output power. Therefore, the efficiency of the IPT system with PDM is very poor at D=0.2, which is close to that of the system with PSM, as shown in Fig. 25. The system with EPDM performs better because it has lower current ripples. Moreover, the efficiency of the system with EPDM and high-PSA active damping method is always slightly higher than that of the IPT system with PDM, but slightly lower than that of the system with EPDM. Although the introduction of PSM reduces the current ripples and conduction losses in the active damping method, it increases the switching losses accordingly. Therefore, the overall efficiency of the system with the active damping method is slightly lower than that of the system with EPDM in most cases. However, the actively damped system may have higher efficiency when the original system has large current/power ripples, as shown in Fig. 21(b) and Fig. 21(f). The above results effectively prove that the system with the active damping method can achieve high efficiency and low current/power ripples in a wide range of output power.

VI. Conclusion

The dynamic characteristics of IPT systems with CVL and CRL are analysed and compared in this paper. It is clearly demonstrated how a system with CVL characteristics has a significantly less damped response than what results from the commonly used CRL model. Therefore, IPT systems with CVL can experience large oscillations in the sending/pickup current amplitude when using the DSM-based (E)PDM. Two general approaches for attenuating such poorly damped oscillations are identified in this paper by utilizing control to increase the damping of the critical mode. First, it is proposed to operate IPT systems with CVL at a slightly sub-resonant frequency to increase the damping. An approach for ensuring maximum improvement of damping while maintaining ZVS with minimum turn-off current of all H-bridge switches is also presented. Then a method for active damping is studied, by utilizing feedback of the sending side current ripple to transiently introduce PSM on the voltage pulses resulting from the PDM. Thus, effective damping of the critical oscillation mode is achieved over a wide range of operating conditions by applying active damping combined with EPDM and off-resonant frequency operation. Time-domain simulations and experiments on a small-scale prototype demonstrate the validity of the analysis and the feasibility of the proposed methods. It is worth noting that the proposed method can also be directly applicable for suppressing current/power oscillations in inductive battery charging systems with other pulse skipping modulations, such as ON-OFF keying modulation [19]-[21].

References

[1] S. Y. Hui, “Planar wireless charging technology for portable electronic products and Qi,” *Proc*. IEEE, vol. 101, no. 6, pp. 1290–1301, Jun. 2013.

[2] C. C. Mi, G. Buja, S. Y. Choi, C. T. Rim, "Modern advances in wireless power transfer systems for roadway powered vehicles," *IEEE Transactions on Industrial Electronics.,* Vol. 63, No. 10, Oct. 2016, pp. 6533-6545.

[3] G. Guidi, J. A. Suul, F. Jenset, and I. Sorfonn, “Wireless charging for ships: high-power inductive charging for battery electric and plug-in hybrid vessels,” *IEEE Electr. Mag.*, vol. 5, no. 3, pp. 22–32, 2017.

[4] Z. U. Zahid, Zakariya M. Dalala, Cong Zheng, Rui Chen, William Eric Faraci, Jih-Sheng Lai, Gianpaolo Lisi, David Anderson, "Modeling and Control of Series-Series Compensated Inductive Power Transfer System," in *IEEE Journal of Emerging and Selected Topics in Power Electronics*, Vol. 3, No. 1, pp. 111-123, March 2015.

[5] Y. Liu, U. K. Madawala, R. Mai, and Z. He, “An optimal multivariable control strategy for inductive power transfer systems to improve efficiency,” *IEEE Trans. Power Electron*., vol. 35, no. 9, pp. 8998–9010, Sep. 2020.

[6] A. Zakerian, S. Vaez-Zadeh and A. Babaki, "A dynamic WPT system with high efficiency and high power factor for electric vehicles," in *IEEE Trans. Power Electron.*, vol. 35, no. 7, pp. 6732-6740, July 2020.

[7] Y. Jiang, L. Wang, Y. Wang, J. Liu, X. Li and G. Ning, "Analysis, Design, and Implementation of Accurate ZVS Angle Control for EV Battery Charging in Wireless High-Power Transfer," in *IEEE Transactions on Industrial Electronics*, vol. 66, no. 5, pp. 4075-4085, May 2019.

[8] Y. Frechter and A. Kuperman, "Output Voltage Range of a Power-Loaded Series–Series Compensated Inductive Wireless Power Transfer Link Operating in Load-Independent Regime," in *IEEE Trans. Power Electron.*, vol. 35, no. 6, pp. 6586-6593, June 2020.

[9] G. Guidi and J. A. Suul, “Modelling techniques for designing high performance on-road dynamic charging systems for electric vehicles,” in *Proc. 31st Int. Electric Vehicle Symposium and Exhibition & Int Electric Vehicle Technology Conf.*, Sep. 2018, pp. 1–7.

[10] E. Torsgård, G. Guidi, J. A. Suul, "Small-signal state-space analysis of inductive battery charging system in off-resonant operation," in *Proceedings of the Twentieth IEEE Workshop on Control and Modelling for Power Electronics*, COMPEL 2019, Toronto, Ontario, Canada, 17-20 June 2019, pp. 1-8.

[11] Keiichiro Tokita, Hiroshi Fujimoto, Yoichi Hori, "Feedforward Transient Control Under Varying Coupling Condition for In-motion Wireless Power Transfer Using Envelope Model", *Wireless Power Transfer Conference (WPTC) 2020 IEEE*, pp. 166-169, 2020.

[12] R. Tavakoli, Z. Pantic, "Analysis, Design, and Demonstration of a 25-kW Dynamic Wireless Charging System for Roadway Electric Vehicles," in *IEEE Journal of Emerging and Selected Topics in Power Electronics*, Vol. 6, No. 3, pp. 1378-1393, September 2018.

[13] J. Zhou, G. Guidi, K. Ljøkelsøy, J. A. Suul, "Analysis and Mitigation of Oscillations in Inductive Power Transfer Systems with Constant Voltage Load and Pulse Density Modulation", in *Proceedings of the Thirteenth Annual IEEE Energy Conversion Congress and Exposition, ECCE 2021, Vancouver, British Columbia*, Canada / Virtual Conference, 10-14 October 2021, pp. 1565-1572.

[14] H. Li, J. Fang, S. Chen, K. Wang, and Y. Tang, “Pulse density modulation for maximum efficiency point tracking of wireless power transfer systems,” *IEEE Trans. Power Electron.*, vol. 33, no. 6, pp. 5492–5501, Jun. 2018.

[15] H. Fujita and H. Akagi, “Pulse-density-modulated power control of a 4 kW450 kHz voltage-source inverter for induction melting applications,” *IEEE Trans. Ind. Appl*., vol. 32, no. 2, pp. 279–286, Mar./Apr. 1996.

[16] V. Esteve et al., “Improving the efficiency of IGBT series-resonant inverters using pulse density modulation,” *IEEE Transactions on Industrial Electronics*, vol. 58, no. 3, pp. 979–987, Mar. 2011.

[17] H. Li, S. Chen, J. Fang, Y. Tang and M. A. de Rooij, "A low-subharmonic full-range and rapid pulse density modulation strategy for ZVS full-bridge converters", *IEEE Trans. Power Electron*., vol. 34, no. 9, pp. 8871-8881, Sep. 2019.

[18] M. Fan, L. Shi, Z. Yin, L. Jiang and F. Zhang, "Improved pulse density modulation for semi-bridgeless active rectifier in inductive power transfer system", *IEEE Trans. Power Electron*., vol. 34, no. 6, pp. 5893-5902, Jun. 2019.

[19] W. Zhong and S. Y. R. Hui, “Maximum energy efficiency operation of series-series resonant wireless power transfer systems using on-off keying modulation,” *IEEE Trans. Power Electron*., vol. 33, no. 4, pp. 3595–3603, Apr. 2018.

[20] U. Anwar, Z. Liu, D. Markovic, "A Burst-Mode Controlled Inductive Wireless Power Transfer System", *Control and Modeling for Power Electronics (COMPEL) 2020 IEEE 21st Workshop on*, pp. 1-6, 2020.
[21] W. Zhong, H. Li, S. Y. R. Hui, M. Dehong Xu, "Current Overshoot Suppression of Wireless Power Transfer Systems With on–off Keying Modulation", *IEEE Trans. Power Electron*., vol. 36, no. 3, pp. 2676-2684, 2021.
[22] G. Guidi and J. A. Suul, "Minimizing converter requirements of inductive power transfer systems with constant voltage load and variable coupling conditions," *IEEE Transactions on Industrial Electronics*, vol. 63, no. 11, pp. 6835–6844, Nov 2016.
[23] Z. U. Zahid et al., "Design and control of a single-stage large air-gapped transformer isolated battery charger for wide-range output voltage for EV applications," in *Proc. 5th Annu. IEEE Energy Convers. Congr. Expo*., Denver, CO, USA, Sep. 15–19, 2013, pp. 5481–5487.
[24] K. Aditya and S. S. Williamson, "Design guidelines to avoid bifurcation in a series–series compensated inductive power transfer system", *IEEE Transactions on Industrial Electronics*, vol. 66, no. 5, pp. 3973-3982, May 2019.
[25] V. Esteve, J. Jordán, E. Sanchis-Kilders, et al. "Enhanced Pulse-Density-Modulated Power Control for High-Frequency Induction Heating Inverters." *IEEE Transactions on Industrial Electronics*, vol. 62, no. 11, pp.6905-6914, Nov. 2015.
[26] S. Li and C. C. Mi, "Wireless Power Transfer for Electric Vehicle Applications," in *IEEE Journal of Emerging and Selected Topics in Power Electronics*, vol. 3, no. 1, pp. 4-17, March 2015.
[27] W. Wu, Y. Liu, Y. He, H. S. Chung, M. Liserre and F. Blaabjerg, "Damping Methods for Resonances Caused by LCL-Filter-Based Current-Controlled Grid-Tied Power Inverters: An Overview," in *IEEE Transactions on Industrial Electronics*, vol. 64, no. 9, pp. 7402-7413, Sept. 2017.
[28] Y. Tang, P. C. Loh, P. Wang, F. H. Choo, F. Gao and F. Blaabjerg, "Generalized design of high performance shunt active power filter with output LCL filter," in *IEEE Transactions on Industrial Electronics*, vol. 59, no. 3, pp. 1443-1452, March 2012.